Liu et al. Nanoscale Research Letters (2017) 12:603
DOI 10.1186/s11671-017-2373-5

Nanoscale Research Letters

NANO EXPRESS Open Access

Pronounced Photovoltaic Response from Multi-layered $MoTe_2$ Phototransistor with Asymmetric Contact Form

Junku Liu[1*], Nan Guo[1], Xiaoyang Xiao[2], Kenan Zhang[3], Yi Jia[1], Shuyun Zhou[3], Yang Wu[2], Qunqing Li[2] and Lin Xiao[1*]

Abstract

In this study, we fabricate air-stable p-type multi-layered $MoTe_2$ phototransistor using Au as electrodes, which shows pronounced photovoltaic response in off-state with asymmetric contact form. By analyzing the spatially resolved photoresponse using scanning photocurrent microscopy, we found that the potential steps are formed in the vicinity of the electrodes/$MoTe_2$ interface due to the doping of the $MoTe_2$ by the metal contacts. The potential step dominates the separation of photoexcited electron-hole pairs in short-circuit condition or with small V_{sd} biased. Based on these findings, we infer that the asymmetric contact cross-section between $MoTe_2$-source and $MoTe_2$-drain electrodes is the reason to form non-zero net current and photovoltaic response. Furthermore, $MoTe_2$ phototransistor shows a faster response in short-circuit condition than that with higher biased V_{sd} within sub-millisecond, and its spectral range can be extended to the infrared end of 1550 nm.

Keywords: $MoTe_2$, Photovoltaic, Interface, Asymmetric

Background

Graphene and similar two-dimensional (2D) materials exist in bulk form as stacks of strongly bonded layers with weak interlayer attraction, allowing itself to be exfoliated into individual, atomically thin layers, which have opened up new possibilities for the exploration of 2D physics as well as that of new material applications [1–9]. Of them, semiconductor transition metal dichalcogenides (TMDs) with the common formula MX_2, where M stands for a transition metal from group VI (M = Mo, W) and X for a chalcogen element (S, Se, Te), exhibit sizeable bandgaps [2, 3, 10, 11]. In addition, these 2D TMD flakes are flexible and free of dangling bonds between adjacent layers [12, 13]. These unique properties make TMDs promising candidates to construct electronic and optoelectronic devices [2–4, 14–17], such as a next-generation field-effect transistor (FET) at sub-10 nm [18], on-chip light-emitting diode [19–21], and Van der Waals heterostructure devices [4, 5].

2H-type molybdenum ditelluride (2H-$MoTe_2$) is one of the typical 2D TMDs, which has an indirect bandgap of 0.83 eV in bulk form [22] and a direct bandgap of 1.1 eV when it is thinned to monolayer [23]. 2H-$MoTe_2$ has been explored for applications in spintronics [24], FET [25–27], photodetector [28–32], and solar cell [33]. Like most 2D materials, electrical metal contacts with 2H-$MoTe_2$ play an important role in realizing high-performance electronic and optoelectronic devices. It has been proven that p-type and n-type contact doping and ohm contact can be realized using suitable contact materials [34–40], and they can, in turn, be used to construct functional devices, such as photovoltaic photodetector [37, 38] and diode [37]. Up to now, the research focus has been concentrated on evaluating and studying metal-semiconductor contacts by comparing various electrode materials, but insufficient attention has been paid to comparing metal-semiconducting contact forms in-depth, for example, the same contact material with asymmetric contact cross-section.

* Correspondence: liujunku@qxslab.cn; xiaolin@qxslab.cn
[1]Nanophotonics and Optoelectronics Research Center, Qian Xuesen Laboratory of Space Technology, China Academy of Space Technology, Beijing 100094, China
Full list of author information is available at the end of the article

In this study, we fabricate air-stable p-type multi-layered $MoTe_2$ phototransistor with asymmetric contact cross-section between $MoTe_2$-source and $MoTe_2$-drain electrodes and investigate its photoresponse using scanning photocurrent at different gate- and source-drain voltages. This study helps to reveal the spatial potential profiles and analyze the impact of contact in the device. Experimental data show that the device has non-zero net photocurrent in short-circuit condition and photovoltaic response. Scanning photocurrent map reveals that strong photocurrent is generated in the vicinity of contact interface in short-circuit condition or with small source-drain voltage (V_{sd}) biased, which indicates the potential steps are formed in the vicinity of the electrodes/$MoTe_2$ interface due to the doping of the $MoTe_2$ by the metal contacts. When biased voltage V_{sd} rises above the potential step, V_{sd} dominates the separation of photoexcited electron-hole pairs and photocurrent ($I_{PC} = I_{sd} - I_{dark}$) peak appears in the center of the device channel. This indicates the asymmetric contact cross-section between $MoTe_2$-source and $MoTe_2$-drain electrodes is the reason to form non-zero net current and photovoltaic response. This finding is helpful to construct photovoltaic photodetector with low power consumption. Finally, we test the time-resolved and wavelength-dependent photocurrent of $MoTe_2$ phototransistor, obtaining sub-millisecond response time and finding that its spectral range can be extended to the infrared end of 1550 nm.

Results and Discussion

We fabricate two back-gated multi-layered $MoTe_2$ phototransistors (D1 and D2) and measure their photoresponse. The device is identified by an optical microscope, and the corresponding $MoTe_2$ thickness and quality are characterized using atomic force microscopy (AFM) and Raman spectrum. All measurements are conducted in ambient condition. Figure 1a shows the optical image (left) and AFM image (right) of D1 (D2 is shown in Additional file 1: Figure S1. The following data are collected from D1 unless otherwise specified, and the data from D2 are shown in Additional file 1). The device consists of source electrode, drain electrode, and channel sample of multi-layered $MoTe_2$ on SiO_2/p^+-Si substrate. SiO_2 film with the thickness of 300 nm is dielectric, and p^+-Si works as a back-gate electrode. The details of D1 are characterized using AFM, which shows that multi-layered $MoTe_2$ straddles source and drain electrodes. The channel length is 10 μm. $MoTe_2$ sample in the channel is about 23 nm thick (height profile is shown in Additional file 1: Figure S2), and the widths of $MoTe_2$-source and $MoTe_2$-drain contact cross-section are 6.5 and 4.8 μm, respectively. Figure 1b shows the Raman spectrum of $MoTe_2$ sample. The characteristics Raman-active modes of A_{1g} (172 cm^{-1}), E^1_{2g} (233 cm^{-1}), and B^1_{2g} (289 cm^{-1}) are clearly observed, confirming the good quality of $MoTe_2$ in the channel.

Electric measurement indicates that multi-layered $MoTe_2$ phototransistor is p-type as shown in Fig. 1c, which is in on-state at negative gate voltage and in off-state at positive gate voltage. The current on-off ratio is 6.8×10^3 when source-drain voltage V_{sd} is 1 V. The field-effect mobility (μ) is 14.8 cm^2/V s according to transfer characteristics. When biased voltage V_{sd} decreases from 1 V to 100 mV, on-current and off-current both decrease, and the on-off ratio is still above

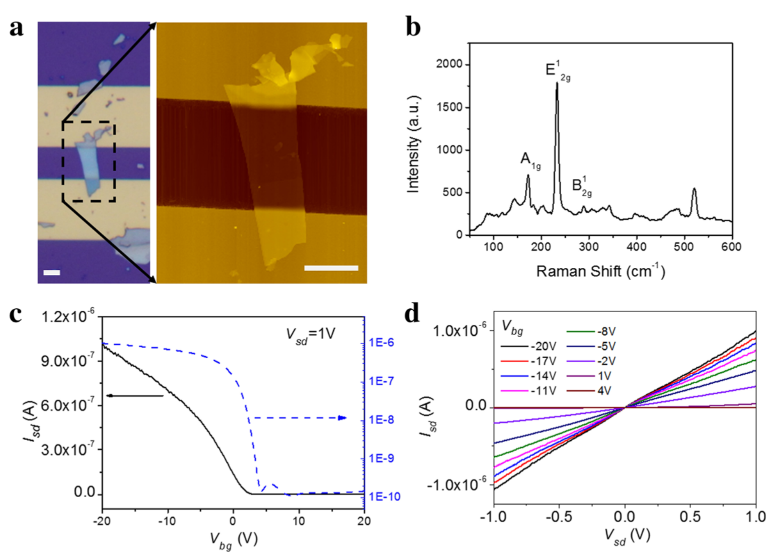

Fig. 1 **a** Optical image and AFM image of multi-layered $MoTe_2$ phototransistor. The scale bars are 5 μm. **b** Raman spectrum of multi-layered $MoTe_2$ phototransistor with 514-nm laser excitation. **c** Transfer characteristics and **d** output characteristics of multi-layered $MoTe_2$ phototransistor

6.0×10^3, as shown in Additional file 1: Figure S3(a) and (b). When the gate voltage is swept from − 20 to 20 V and then back to − 20 V, multi-layered $MoTe_2$ phototransistor shows small hysteresis (see Additional file 1: Figure S3(c)) and air-stable p-type conductance, which benefits from the simple fabrication process and polymer-free $MoTe_2$ sample. We also fabricate other multi-layered $MoTe_2$ phototransistor with a thickness of 5, 10, 11, 12, 15.7, and 38 nm, respectively, as shown in Additional file 1: Figure S4. They all show air-stable p-type conductance. Figure 1d shows the output characteristics of multi-layered $MoTe_2$ transistor as back-gate voltage (V_{bg}) varies from − 20 to 4 V. As seen, the response is essentially linear, especially at a low biased voltage of V_{sd}, which indicates that there is a low Schottky barrier between Au and $MoTe_2$ in the air.

Figure 2 shows the photoresponse of multi-layered $MoTe_2$ phototransistor when it is illuminated by 637-nm continuous-wave laser in ambient condition, which is conducted by combining Agilent B1500A semiconductor analyzer with Lakeshore probe station. Laser spot size is larger than 200 μm in diameter, and the device is covered with uniform illumination intensity. Backgate-dependent and power-dependent photoresponse are shown in Additional file 1: Figure S5. As shown in Fig. 2a, when a back-gate voltage is 0 V, source-drain current (I_{sd}) increases with laser power. I_{sd} vs. V_{sd} curves at different illumination power levels all meet at $V_{sd} = 0$ V, which is clearly observed in a logarithmic plot of $|I_{sd}|$ shown in insert Figure of Fig. 2a. When $V_{bg} = 5$ V, the phototransistor is in off-state (see Fig. 1c), and the current of I_{sd} increases with the illumination laser power, exhibiting clear nonlinear behavior, as shown in Fig. 2b. Furthermore, the phototransistor shows non-zero open-circuit voltage (V_{OC}) and short-circuit current (I_{SC}) with laser illumination, which is the evidence of photovoltaic response from multi-layered $MoTe_2$ phototransistor. Figure 2c shows V_{OC} and I_{SC} as a function of illumination power. V_{OC} remains unchanged at 50 mV (illumination power is higher than 500 μW), and $|I_{SC}|$ increases from 0 to 1.6 nA when laser power increases from 0 to 4175 μW. When we change the voltage direction, V_{OC} and I_{SC} remain unchanged as shown in Fig. 2d. V_{sd} represents the voltage loaded on source electrode and V_{ds} is loaded on drain electrode, and the corresponding current is indicated by I_{sd} and I_{ds}, respectively. Insert image in Fig. 2d illustrates the voltage and current direction. Whether the voltage is loaded on the source or drain electrode, the V_{OC} of 50 mV relative to source voltage and corresponding I_{SC} of 680 pA flowing from drain electrode to source electrode both remain unchanged. This confirms the photovoltaic response of multi-layered $MoTe_2$ phototransistor.

In order to reveal the mechanism of photoresponse, especially the photovoltaic response, we perform a scanning photocurrent microscopy (SPCM) study, which helps to obtain the spatial potential profiles and to analyze the spatially resolved photoresponse. SPCM is performed using a home-made scanning photocurrent setup in ambient condition. Optical excitation is provided by SuperK EXTREME supercontinuum white light laser. Its wavelength ranges from 400 to 2400 nm. The beam, with adjustable wavelength using SuperK SELECT multi-line tunable filter, is focused on the device using a 20× objective lens. A galvanometer mirror positioning

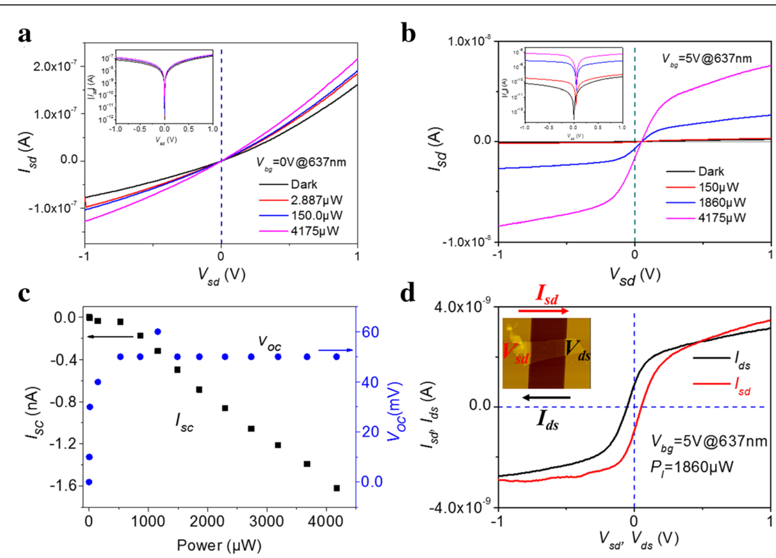

Fig. 2 Photoresponse of multi-layered $MoTe_2$ phototransistor illuminated by 637-nm wavelength laser in ambient condition. **a** I_{sd} vs. V_{sd} curves at $V_{bg} = 0$ V as illumination power increases. **b** I_{sd} vs. V_{sd} curves at $V_{bg} = 5$ V as illumination power increases. **c** V_{OC} and I_{SC} as a function of illumination power. **d** Output current for biased voltage loaded on the source and drain electrode, respectively

system is used to make the laser beam scan the device to obtain photocurrent maps. The reflected light and the photocurrent are recorded with a current preamplifier and a lock-in amplifier at chopper frequency of 1 KHz.

Figure 3 shows the scanning photocurrent of D1 with an excitation wavelength of 1200 nm. Laser spot diameter is about 4.4 μm derived from the reflection image (see Additional file 1: Figure S7). Figure 3a shows the optical image, together with the electrical setup. I_{PC} measurements are conducted in short-circuit condition, in which source electrode is grounded and I_{PC} is collected from drain electrode. The current flowing from the source to drain electrode is positive. Figure 3b shows spatial-resolved photocurrent image collected at the gate voltage (V_{bg}) of − 5, 0, and 5 V, respectively. It can be seen that short-circuit I_{PC} with opposite polarities is strong in the vicinity of the interfaces between $MoTe_2$ and the electrodes. When V_{bg} is changed from − 5 to 0 V, I_{PC} pattern remains unchanged but the intensity decreases. V_{bg} is further increased to 5 V; I_{PC} not only switches polarity, the position of maximum I_{PC} also moves away from contact interface and into the channel. Figure 3c shows the I_{PC} profile taken from the black dashed line in Fig. 3b at $V_{bg} = -5$, 0, and 5 V, respectively. It clearly demonstrates that I_{PC} has a broad intensity peak near the interface between $MoTe_2$ and electrodes at $V_{bg} = -5$ and 0 V, while the peak moves into the channel, which is about 3 μm away from the contact interface and becomes narrower.

The presence of I_{PC} peaks indicates the existence of potential steps in short-circuit condition. According to the I_{PC} distribution, we plot the corresponding potential profile along the device channel as shown in Fig. 3d. At $V_{bg} = -5$ and 0 V, the potential steps are near the contact interface between $MoTe_2$ and electrodes, and they move into the channel at $V_{bg} = 5$ V. According to the previous study [41], Au electrode contact introduces p-doping and pins the Fermi level of $MoTe_2$ at contact part. Thus, the potential steps are formed in the vicinity of the electrode/$MoTe_2$ interface as the Fermi level in the channel is modulated by the gate voltage. At $V_{bg} = 0$ V, a weak I_{PC} is observed, which flows from the electrode to $MoTe_2$ channel. It means photoexcited electrons drift to nearby electrode and holes to $MoTe_2$ channel. At $V_{bg} = -5$ V, the hole density in $MoTe_2$ channel is enhanced and induces a larger potential step in the vicinity of the electrode/$MoTe_2$ interface. Photoexcited electron-hole pairs can be separated effectively and I_{PC} increases. When $V_{bg} = 5$ V, more electrons are injected into the $MoTe_2$ channel, and potential well is formed in the channel. Because of electrostatics of electrode, the potential steps move away from the electrode and appear in the channel. The photoexcited electrons drift to the $MoTe_2$ channel and holes toward the nearby electrode. I_{PC} changes direction compared with that at $V_{bg} = -5$ and 0 V.

Figure 4 shows the spatial-resolved I_{PC} at different V_{sd} as $V_{bg} = 0$ and 5 V, respectively. Figure 4a shows the optical image, together with the electrical setup. V_{sd} is loaded on the source electrode, and I_{PC} is collected from the drain electrode. The current flowing from the source to drain electrode is positive. Figure 4b shows I_{PC} as a function of V_{sd} at $V_{bg} = 0$ V. When $V_{sd} = 0$, − 0.01, and 0.01 V, strong I_{PC} occurs in the vicinity of $MoTe_2$/electrodes interface, then it moves toward the channel center as V_{sd} increases to 0.1 V. Similar trend is observed at $V_{bg} = 5$ V as V_{sd} increases as shown in Fig. 4c. Figure 4d shows a clear I_{PC} peak in the center of the device channel as V_{sd} increases to 0.5 V. I_{PC} profiles taken along the black dashed line in Fig. 4a are shown in Fig. 4e, f, which clearly show the I_{PC} variation trend as V_{sd} increases. They both indicate the maximum I_{PC} generated in the vicinity of contact interface in short-circuit condition or with small V_{sd} biased. When the biased voltage is increased, photocurrent peak moves toward the center of the device channel.

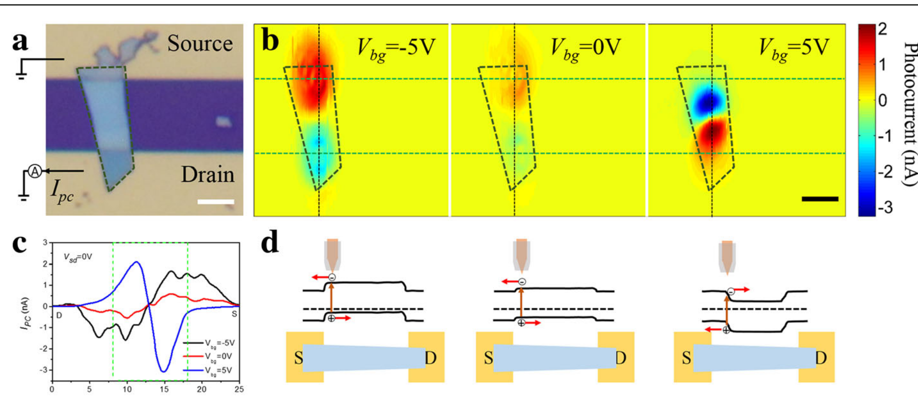

Fig. 3 Spatial-resolved photocurrent images of D1 as a function of gate voltage. **a** The optical image together with the electrical setup. **b** Spatial-resolved photocurrent images at $V_{bg} = -5$, 0, and 5 V, respectively. **c** I_{PC} profile collected from the black dashed line in Fig. 3b. **d** Corresponding potential profiles at $V_{bg} = -5$, 0, and 5 V, respectively. The scale bars are 5 μm in all figures

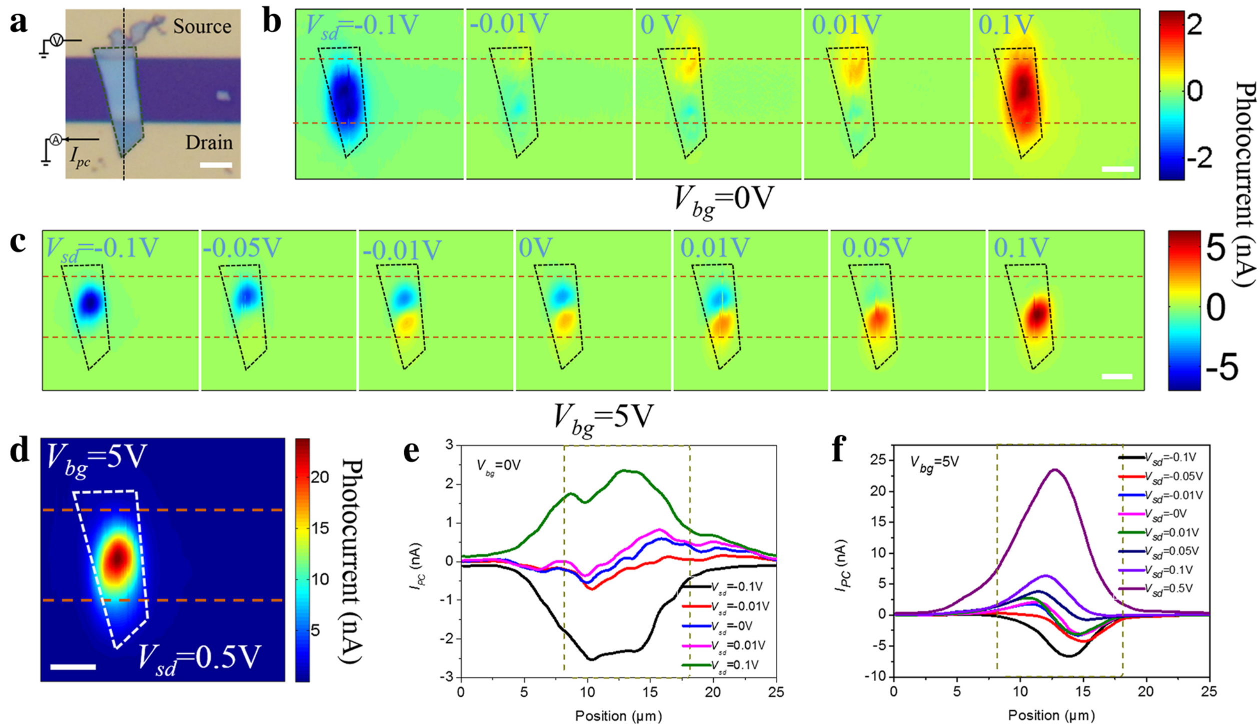

Fig. 4 Spatial-resolved photocurrent images of D1 as a function of V_{sd}. **a** The optical image together with the electrical setup. **b** Spatial-resolved photocurrent images at $V_{bg} = 0$ V and $V_{sd} = -0.1$, 0.01, 0, 0.01, and 0.1 V, respectively. **c** Spatial-resolved photocurrent images at $V_{bg} = 5$ V and V_{sd} varies from -0.1 to 0.1 V. **d** Spatial-resolved photocurrent images at $V_{bg} = 5$ V and $V_{sd} = 0.5$ V. **e** I_{PC} profile at $V_{bg} = 0$ V and **f** I_{PC} profile at $V_{bg} = 5$ V taken along dashed line in Fig. 4a. The scale bars are 5 μm in all figures

Based on these findings, we know that the potential step, formed in the vicinity of the electrodes/$MoTe_2$ interface due to the doping of the $MoTe_2$ by the metal contacts, dominates the separation of photoexcited electron-hole pairs in short-circuit condition or with small V_{sd} biased. Thus, I_{PC} at $MoTe_2$-source is larger than that at $MoTe_2$-drain due to the larger contact interface at $MoTe_2$-source, and the net current is not zero, while the non-zero net current is smaller than I_{sd} at $V_{bg} = -5$ and 0 V (in on-state), and larger than that at $V_{bg} = 5$ V (in off-state). Therefore, we observe clear I_{SC} at $V_{bg} = 5$ V as shown in Fig. 2b and Additional file 1: Figure S6(b)–(f). Therefore, both I_{SC} and the corresponding V_{OC} are the results of the potential step and asymmetric contact. Furthermore, we fabricate D2 sample with more asymmetric contact cross-section, as shown in Additional file 1: Figure S1, compared with D1. It shows a similar photovoltaic response, with V_{OC} as high as 150 mV when $V_{bg} = 5$ V and illumination laser wavelength is 637 nm. When the illumination wavelength varies to 830, 940, 1064, and 1312 nm, D2 shows a similar photovoltaic response at $V_{bg} = 5$ V (see Additional file 1: Figure S6). We also fabricate other four devices as shown in Additional file 1: Figure S8, they demonstrate the similar behavior to that has been shown in D1 and D2. These data further confirm that photovoltaic response of multi-layered $MoTe_2$ phototransistor is a result from the asymmetric contact cross-section between $MoTe_2$-source and $MoTe_2$-drain electrodes.

Finally, we test the photoresponse time and spectral range of multi-layered $MoTe_2$ phototransistor. Figure 5a shows the time-resolved photocurrent at $V_{bg} = 5$ V and $V_{sd} = 0$ and 1 V, respectively, which are recorded using a current preamplifier and oscilloscope. The excitation laser is a square wave with 2 ms width at 637 nm wave-length. The currents collected under $V_{sd} = 0$ and 1 V show opposite direction, which is consistent with the data given in Fig. 2b, and is a result from the difference between V_{OC} and V_{sd}. The rise time and fall time of photoresponse are defined as the time between 10 and 90% of the total photocurrent. As seen, the rise time (τ^0_{rise}) is 20 μs and fall time (τ^0_{fall}) is 127 μs at $V_{sd} = 0$ V, and the rise time (τ^1_{rise}) is 210 μs and fall time (τ^1_{fall}) is 302 μs at $V_{sd} = 1$ V, which are both larger than that at $V_{sd} = 0$ V. This is because of the different mechanism of photocurrent generation. At $V_{sd} = 0$ V, the potential step-dominated photocurrent is generated in the vicinity of electrode/$MoTe_2$ interface. At $V_{sd} = 1$ V, the photocurrent is generated in the device channel, and the photoexcited carriers have to go through the channel to arrive at the electrode, which takes longer time than the generation near the electrode/$MoTe_2$ interface. Thus, the device shows longer photoresponse time at $V_{sd} = 1$ V than that at $V_{sd} = 0$ V.

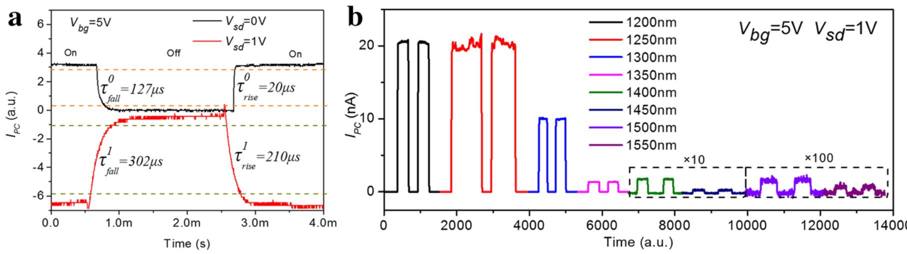

Fig. 5 Photoresponse time and spectral range of multi-layered $MoTe_2$ phototransistor. **a** Time-resolved photocurrent at $V_{bg} = 5$ V and $V_{sd} = 0$ V (black line) and 1 V (red line), respectively. **b** Photoresponse at different photoexcitation wavelengths

In addition to working at the visible band, a multi-layered $MoTe_2$ phototransistor has photoresponse at the near-infrared band. Figure 5b shows that its photoresponse can be extended from 1200 to 1550 nm. Optical excitation, provided by SuperK EXTREME supercontinuum white light laser, is focused on the device channel center using a 20× objective lens with a spot diameter of 4.4 μm. The data indicate that multi-layered $MoTe_2$ phototransistor can be used in the communication band.

Conclusions

In summary, we have fabricated air-stable p-type multi-layered $MoTe_2$ phototransistor with asymmetric contact form. Its photoresponse is investigated using scanning photocurrent at different gate and source-drain voltages, which helps to reveal the spatial potential profiles. The results indicate that potential step, formed in the vicinity of the electrodes/$MoTe_2$ interface due to the doping of the $MoTe_2$ by the metal contacts, plays an important role in separating photoexcited electron-hole pairs in short-circuit condition or with small V_{sd} biased. Net current is non-zero when potential step exists with asymmetric contact cross-section between $MoTe_2$-source and $MoTe_2$-drain electrodes. When biased voltage V_{sd} rises above potential step, V_{sd} dominates the separation of photoexcited electron-hole pairs, and I_{PC} peak appears in the center of the device channel. Moreover, $MoTe_2$ phototransistor shows a faster response in short-circuit condition than that with higher biased V_{sd} within sub-millisecond, and its spectral range can be extended to the infrared end of 1550 nm.

Methods/Experimental

Back-gated multi-layered $MoTe_2$ phototransistors are fabricated in the following way. First, source, drain, and gate electrodes are patterned on 300-nm SiO_2/p^+-Si substrate using standard UV photolithography techniques, followed by selective etching of 300-nm SiO_2 beneath the gate electrode and E-beam evaporation of a 5 nm/100 nm Cr/Au films. Second, the multi-layered $MoTe_2$ sample is prepared on another 300-nm SiO_2/p^+-Si substrate by mechanical exfoliation of mm-size semiconducting 2H-$MoTe_2$ single crystals, which is grown by chemical vapor transport using $TeCl_4$ as the transport agent in a temperature gradient of 750 to 700 °C for 3 days. Finally, the prepared multi-layered $MoTe_2$ sample is transferred onto patterned source-drain electrodes using polyvinyl alcohol (PVA) as a medium. PVA is dissolved in H_2O and rinsed with isopropyl alcohol. Multi-layered $MoTe_2$ samples are identified by an optical microscope, and the corresponding thickness is characterized using SPA-300HV atomic force microscopy (AFM). Raman signals are collected by a LabRAM HR Raman spectrometer with 514-nm wavelength laser excitation in the backscattering configuration using a 100 × objective.

Electrical characterization and photoresponse for 637-nm laser excitation are performed by combining Agilent B1500A semiconductor analyzer with Lakeshore probe station. The laser is illuminated onto the device using fiber and, the spot size is larger than 200 μm. Time-resolved photocurrent is recorded using a DL1211 current preamplifier and Keysight MSOX3024T oscilloscope. Spatial-resolved photocurrent is conducted using a home-made setup. The excitation laser is provided by SuperK EXTREME supercontinuum white light laser with an accessory of SuperK SELECT multi-line tunable filter to adjust the wavelength. The light is focused onto the device using a 20× objective lens and is chopped with SR570. The reflected light and the photocurrent are recorded with DL1211 current preamplifier and SR830 lock-in amplifier.

Additional file

Additional file 1: Figure S1. D2 properties. **Figure S2.** AFM image and corresponding height profile D1. **Figure S3.** Electric properties of D1. **Figure S4.** Electric properties of $MoTe_2$ phototransistor with different thickness. **Figure S5.** Backgate-dependent and power-dependent photoresponse of D1. **Figure S6.** Photoresponse of D2 with different excitation wavelength. **Figure S7.** Normalized reflection in the vicinity of electrode. **Figure S8.** The photoresponse of other four multi-layered $MoTe_2$ phototransistors. (DOCX 1617 kb)

Abbreviations

2D: Two-dimensional; 2H-$MoTe_2$: 2H-type molybdenum ditelluride; AFM: Atomic force microscopy; FET: Field-effect transistor; I_{PC}: Photocurrent; I_{SC}: Short-circuit current; I_{sd}: Source-drain current; PVA: Polyvinyl alcohol;

TMDs: Transition metal dichalcogenides; V_{bg}: Back-gate voltage; V_{OC}: Open-circuit voltage; V_{sd}: Source-drain voltage; τ_{fall}: Fall time; τ_{rise}: Rise time

Acknowledgements
This work was financially supported by National Natural Science Foundation of China (51502337, 11574171, and 51472019) and Open Research Fund Program of the State Key Laboratory of Low-Dimensional Quantum Physics.

Availability of data and materials
The datasets supporting the conclusions of this article are included within the article and its supporting information.

Authors' contributions
JL and LX conceived the experiment. JL designed the experiment, performed the measurements, and drafted the manuscript. XX performed the transport measurements with the assistance of YJ, NG, and LX. KZ grown 2H-$MoTe_2$ single crystals with the assistance of YW and SZ. All authors discussed the results and approved the final manuscript.

Funding
National Natural Science Foundation of China (51502337, 11574171, and 51472019) and Open Research Fund Program of the State Key Laboratory of Low-Dimensional Quantum Physics

Competing interests
The authors declare that they have no competing interests.

Publisher's Note

Author details
[1]Nanophotonics and Optoelectronics Research Center, Qian Xuesen Laboratory of Space Technology, China Academy of Space Technology, Beijing 100094, China. [2]State Key Laboratory of Low-Dimensional Quantum Physics, Department of Physics and Tsinghua-Foxconn Nanotechnology Research Center, Tsinghua University, Beijing 100084, China. [3]Department of Physics, Tsinghua University, Beijing 100084, China.

Received: 15 October 2017 Accepted: 14 November 2017
Published online: 22 November 2017

References

1. Novoselov KS, Jiang D, Schedin F et al (2005) Two-dimensional atomic crystals. Proc Natl Acad Sci U S A 102:10451–10453. https://doi.org/10.1073/pnas.0502848102
2. Mak KF, Shan J (2016) Photonics and optoelectronics of 2D semiconductor transition metal dichalcogenides. Nat Photonics 10:216–226. https://doi.org/10.1038/ nphoton.2015.282
3. Wang QH, Kalantar-Zadeh K, Kis A et al (2012) Electronics and optoelectronics of two-dimensional transition metal dichalcogenides. Nat Nanotechnol 7:699–712. https://doi.org/10.1038/nnano.2012.193
4. Liu Y, Weiss NO, Duan X et al (2016) Van der Waals heterostructures and devices. Nat Rev Mater 1:16042. https://doi.org/10.1038/natrevmats.2016.42
5. Geim AK, Grigorieva IV (2013) Van der Waals heterostructures. Nature 499: 419–425. https://doi.org/10.1038/nature12385
6. Bhimanapati GR, Lin Z, Meunier V et al (2015) Recent advances in two-dimensional materials beyond graphene. ACS Nano 9:11509–11539. https://doi.org/10.1021/acsnano.5b05556
7. Butler SZ, Hollen SM, Cao L et al (2013) Progress, challenges, and opportunities in two-dimensional materials beyond graphene. ACS Nano 7: 2898–2926. https://doi.org/10.1021/nn400280c
8. Novoselov KS, Mishchenko A, Carvalho A, Neto AHC (2016) 2D materials and van der Waals heterostructures. Science 353:aac9439. https://doi.org/10.1126/ science.aac9439
9. Chhowalla M, Jena D, Zhang H (2016) Two-dimensional semiconductors for transistors. Nat Rev Mater 1:16052. https://doi.org/10.1038/natrevmats.2016.52
10. Mak KF, Lee C, Hone J et al (2010) Atomically thin MoS_2: a new direct-gap semiconductor. Phys Rev Lett 105:136805. https://doi.org/10.1103/PhysRevLett.105. 136805
11. Splendiani A, Sun L, Zhang Y et al (2010) Emerging photoluminescence in monolayer MoS2. Nano Lett 10:1271–1275. https://doi.org/10.1021/nl903868w
12. Chhowalla M, Shin HS, Eda G et al (2013) The chemistry of two-dimensional layered transition metal dichalcogenide nanosheets. Nat Chem 5:263–275. https://doi.org/10.1038/nchem.1589
13. Velusamy DB, Kim RH, Cha S et al (2015) Flexible transition metal dichalcogenide nanosheets for band-selective photodetection. Nat Commun 6:8063. https://doi.org/10.1038/ncomms9063
14. Wang Q, Cai K, Li J et al (2016) Rational design of ultralarge $Pb_{1-x}Sn_xTe$ nanoplates for exploring crystalline symmetry-protected topological transport. Adv Mater 28:617–623. https://doi.org/10.1002/adma.201504630
15. He L, Xiu F, Wang Y et al (2011) Epitaxial growth of Bi_2Se_3 topological insulator thin films on Si (111). J Appl Phys 109:103702. https://doi.org/10.1063/ 1.3585673
16. Yin L, Xu K, Wen Y et al (2016) Ultrafast and ultrasensitive phototransistors based on few-layered $HfSe_2$. Appl Phys Lett 109:213105. https://doi.org/10.1063/ 1.4968808
17. Buscema M, Island JO, Groenendijk DJ et al (2015) Photocurrent generation with two-dimensional van der Waals semiconductors. Chem Soc Rev 44: 3691–3718. https://doi.org/10.1039/C5CS00106D
18. Nourbakhsh A, Zubair A, Sajjad RN et al (2016) MoS_2 field-effect transistor with sub-10 nm channel length. Nano Lett 16:7798–7806. https://doi.org/10.1021/acs.nanolett.6b03999
19. Ross JS, Klement P, Jones AM et al (2014) Electrically tunable excitonic light-emitting diodes based on monolayer WSe_2 p-n junctions. Nat Nanotechnol 9:268–272. https://doi.org/10.1038/nnano.2014.26
20. Withers F, Del Pozo-Zamudio O, Mishchenko A et al (2015) Light-emitting diodes by band-structure engineering in van der Waals heterostructures. Nat Mater 14:301–306. https://doi.org/10.1038/nmat4205
21. Cheng R, Li D, Zhou H et al (2014) Electroluminescence and photocurrent generation from atomically sharp WSe_2/MoS_2 heterojunction p–n diodes. Nano Lett 14:5590–5597. https://doi.org/10.1021/nl502075n
22. Chen B, Sahin H, Suslu A et al (2015) Environmental changes in $MoTe_2$ excitonic dynamics by defects-activated molecular interaction. ACS Nano 9: 5326–5332. https://doi.org/10.1021/acsnano.5b00985
23. Ruppert C, Aslan OB, Heinz TF (2014) Optical properties and band gap of single- and few-layer $MoTe_2$ crystals. Nano Lett 14:6231–6236. https://doi.org/10.1021/nl502557g
24. Xiao D, Liu G-B, Feng W et al (2012) Coupled spin and valley physics in monolayers of MoS_2 and other group-VI dichalcogenides. Phys Rev Lett 108: 196802. https://doi.org/10.1103/PhysRevLett.108.196802
25. Pradhan NR, Rhodes D, Feng S et al (2014) Field-effect transistors based on few-layered α-$MoTe_2$. ACS Nano 8:5911–5920. https://doi.org/10.1021/nn501013c
26. Lin Y-F, Xu Y, Wang S-T et al (2014) Ambipolar $MoTe_2$ transistors and their applications in logic circuits. Adv Mater 26:3263–3269. https://doi.org/10.1002/ adma.201305845
27. Fathipour S, Ma N, Hwang WS et al (2014) Exfoliated multilayer $MoTe_2$ field-effect transistors. Appl Phys Lett 105:192101. https://doi.org/10.1063/1.4901527
28. Octon TJ, Nagareddy VK, Russo S et al (2016) Fast high-responsivity few-layer $MoTe_2$ photodetectors. Adv Opt Mater 4:1750–1754. https://doi.org/10.1002/adom.201600290
29. Huang H, Wang J, Hu W et al (2016) Highly sensitive visible to infrared $MoTe_2$ photodetectors enhanced by the photogating effect. Nanotechnology 27:445201. https://doi.org/10.1088/0957-4484/27/44/445201
30. Zhang K, Zhang T, Cheng G et al (2016) Interlayer transition and infrared photodetection in atomically thin type-II $MoTe_2/MoS_2$ van der Waals heterostructures. ACS Nano 10:3852–3858. https://doi.org/10.1021/acsnano.6b00980
31. Wang J, Fang H, Wang X et al (2017) Recent progress on localized field enhanced two-dimensional material photodetectors from ultraviolet—visible to infrared. Small 13:1700894. https://doi.org/10.1002/smll.201700894
32. Yin L, Zhan X, Xu K et al (2016) Ultrahigh sensitive $MoTe_2$ phototransistors driven by carrier tunneling. Appl Phys Lett 108:043503. https://doi.org/10.1063/ 1.4941001
33. Pezeshki A, Shokouh SHH, Nazari T et al (2016) Electric and photovoltaic behavior of a few-layer α-$MoTe_2/MoS_2$ dichalcogenide

heterojunction. Adv Mater 28:3216–3222. https://doi.org/10.1002/adma.201504090
34. Leong WS, Luo X, Li Y et al (2015) Low resistance metal contacts to MoS_2 devices with nickel-etched-graphene electrodes. ACS Nano 9:869–877. https://doi.org/10.1021/nn506567r
35. Xu Y, Cheng C, Du S et al (2016) Contacts between two- and three-dimensional materials: ohmic, Schottky, and p–n heterojunctions. ACS Nano 10:4895–4919. https://doi.org/10.1021/acsnano.6b01842
36. Liu W, Kang J, Sarkar D et al (2013) Role of metal contacts in designing high-performance monolayer n-type WSe_2 field effect transistors. Nano Lett 13:1983–1990. https://doi.org/10.1021/nl304777e
37. Lee C-H, Lee G-H, van der Zande AM et al (2014) Atomically thin p–n junctions with van der Waals heterointerfaces. Nat Nanotechnol 9:676–681. https://doi.org/10.1038/nnano.2014.150
38. Mueller T, Xia F, Avouris P (2010) Graphene photodetectors for high-speed optical communications. Nat Photonics 4:297–301. https://doi.org/10.1038/nphoton. 2010.40
39. Lee EJH, Balasubramanian K, Weitz RT et al (2008) Contact and edge effects in graphene devices. Nat Nanotechnol 3:486–490. https://doi.org/10.1038/nnano.2008.172
40. Mueller T, Xia F, Freitag M et al (2009) Role of contacts in graphene transistors: a scanning photocurrent study. Phys Rev B 79:245430. https://doi.org/10.1103/PhysRevB. 79.245430
41. Kim C, Moon I, Lee D et al (2017) Fermi level pinning at electrical metal contacts of monolayer molybdenum dichalcogenides. ACS Nano 11:1588–1596. https://doi.org/10.1021/acsnano.6b07159